

Universitat Autònoma de Barcelona
Institut de Ciència de Materials de Barcelona (ICMAB-CSIC)
Nanopto

On Improving the Efficiency of Organic Photovoltaic Devices: Novel Strategies

Martí Gibert Roca

Under the supervision and tutoring of:

Mariano Campoy Quiles

Submitted in part fulfilment of the requirements
for the degree of Doctor of Philosophy in Materials Science
of the Universitat Autònoma de Barcelona, February 2022

Abstract

Recent advances in Organic Photovoltaics have brought this field to the forefront of renewable energy research. Organic photovoltaic devices have gained plenty of attention thanks to their chemical tunability, light weight, flexibility and increasing efficiency. Being roll-to-roll compatible, the manufacturing processes needed to produce such devices are easily scalable, and their low material usage and low embedded energy make for a sustainable commercial technology that can contribute to solve our current energy crisis. This technology, however, still faces several obstacles that prevent its widespread development. On the one hand, low charge mobilities and relatively modest absorption coefficients limit the final solar cell efficiency, while the complex synthetic routes of the best performing materials limit their economic viability. On a device level, the technology faces different issues related to limited thermal stabilities, as well as tandem fabrication difficulties, to name but a few.

This thesis explores three novel strategies focused on improving the overall efficiency of organic photovoltaic devices, specifically designed to increase light absorption, enhance charge carrier mobility and reduce thermalization losses. In order to tackle such an ambitious research program, we first developed a characterization platform that enabled us to measure organic photovoltaic devices in a highly reproducible manner and between 5 and 10 times faster than sequential methods. This platform consists in the combination of hardware and software that enables any user to characterize a photovoltaic device in a fully automated procedure reducing human errors, homogenizing the results amongst all different users, and saving a significant amount of time and effort. This platform is described in Chapter ??, with further developments also included in other chapters. After this technological chapter, the thesis then details the three approaches to improve efficiency.

Chapter ?? demonstrates the incorporation of photonic structures within photovoltaic devices as means to increase absorption. Specifically, we show that the charge transfer state absorption of organic photovoltaic devices based on P3HT:PC₆₁BM and PBTTT:PC₇₁BM, can be enhanced by nanostructuring their active layer in the shape of a 2D photonic crystal. This absorption enhancement results in an increased EQE, which is especially pronounced below the band gap of the blend. While the improvement is modest for solar cells, this technology results in high

performing infrared photodetectors.

Chapter ?? is based on the hypothesis that charge carrier mobility can be increased by raising photoactive material temperature. To evaluate this, we monitor solar cell performance as a function of active layer temperature. We show that the power conversion efficiency (PCE) is enhanced with temperature, and this effect is especially pronounced on thicker active layers, as one may expect if mobility was the limiting performance. We studied the performance of 10 different photoactive blends at different temperatures, noting that only some of those systems exhibit reversible changes with temperature. In order to understand this behaviour, we investigated in more detail devices made of PBDBT:ITIC, showing that this system has a temperature resistant microstructure and greatly improved charge transport at high temperatures, ultimately translated to better PCE. To perform these experiments, we designed and manufactured a custom experimental setup that is able to characterize our devices, while accurately controlling the active layer temperature.

Finally, the last two chapters demonstrate the feasibility of a, seemingly unexplored, tandem solar cell concept based on spectral splitting, which we named RAINBOW solar cell. This architecture combines a wavelength dispersive optical element and a monolithic in plane (c.f. stack in normal tandem) multi-cell layout with a discrete E_g gradient. In Chapter ?? we study this geometry from a theoretical point of view, performing simulations and calculations with ideal and real materials that establish the scaffolding of RAINBOW solar cell theory, as well as guidelines for material selection. While in Chapter ?? we build an experimental setup capable of characterizing and optimizing real RAINBOW solar cells. The calculations and real measurements are in good agreement, with RAINBOW solar cells providing up to 34% higher efficiency than the best performing sub-cell. As a final proof of concept, we developed partial deposition techniques to manufacture a fully functional monolithic horizontal tandem RAINBOW device.

Contents

Abstract	i
Chapter 1: Materials and Methods	1
1.1 Organic Solar Cell Fabrication	2
1.1.1 Materials	3
1.1.2 Cleaning	6
1.1.3 Blade Coating Deposition	7
1.1.4 Spin Coating Deposition	10
1.1.5 Thermal Evaporation	12
1.1.6 Encapsulation	13
1.1.7 Thermal Annealing	14
1.2 Nanoimprinting Lithography	14
1.2.1 Thermal Nanoimprinting Lithography	15
1.2.2 Solvent Assisted Nanoimprinting Lithography	17
1.2.3 Stamp Fabrication and Architecture	18
1.2.4 Stamp Feature Depth	20
1.3 Device Characterization	20
1.3.1 Electrical Characterization	21
1.3.2 Optical Characterization	23
1.3.3 Topological Characterization	25
Bibliography	1

Chapter 1


Materials and Methods

Abstract

This chapter describes the general procedures used in the fabrication and characterization of the various devices manufactured within this thesis. More specifically, it focuses on solar cell fabrication and characterization, including used materials, manufacturing techniques, and characterization equipment. Special emphasis is placed on the modified solution-process techniques developed within our group, used to manufacture both extremely thick active layers and devices with a thickness gradient in the active layer. The latter is especially advantageous for the manufacturing of a wide range of active layer thickness within one device, resulting in reduced material usage and accelerated device optimization. On the other hand, this chapter also describes the procedures used to manufacture NanoImprinting Lithography (NIL) stamps and their role in solar cell and photodetector active layer nanostructuring, further discussed in Chapter ???. Finally, the characterization section is focused on the explanation of generally available techniques, while novel measurement procedures developed within the scope of this thesis have been thoroughly described within their corresponding chapters.

The objective of this chapter is not to deeply instruct the reader on each process and technique, but rather to provide them with brief explanations that can be useful in understanding unfamiliar methods. In that regard, we have chosen to add details and explanations about most methods and techniques used throughout this thesis, to make it accessible to wider audiences, and for the sake of completeness.

1.1 Organic Solar Cell Fabrication

In this work we have focused on devices fabricated using the inverted architecture  where the transparent electrode is in contact with the ETL, and the top metallic electrode contacts the HTL. However, because the general fabrication procedure is really similar in both conventional and inverted architectures, and since we have manufactured some conventional architecture devices during the course of this thesis, the general materials and methods will be described independently of device architecture, except in the specific steps that are architecture dependent.

As we can see in Figure 1.1, solar cell fabrication begins with an ITO covered glass substrate, which needs to be cleaned, according to the standard **cleaning protocol**. On top of the cleansed ITO layer, we deposit the first **charge selective layer** (ETL for inverted, and HTL for conventional architecture) via solution processing, using different materials and deposition techniques, further explained in later sections according to the specific device. After the charge selective layer, a **photoactive layer** is deposited, also with solution processing techniques, using a wide variety of materials specified within each chapter. In the case of nanostructured devices, **nanoimprinting lithography** is performed on the active layer, either directly after deposition or after the solvent has had time to completely evaporate. On top of these layers, the second **charge transport layer** (HTL for inverted, and ETL for conventional architecture), and the **back electrode** (high work function metal for inverted, and low work function metal for conventional architecture) are deposited via thermal evaporation.

Most devices require an extra step involving the **encapsulation** of the entire device to prevent environment related degradation, as well as a **thermal annealing** that modifies their crystalline properties.

After a device is completely finished, it is thoroughly **characterized** by using a variety of techniques that help us determine their electrical and optical performance, as well as their basic topographical characteristics.

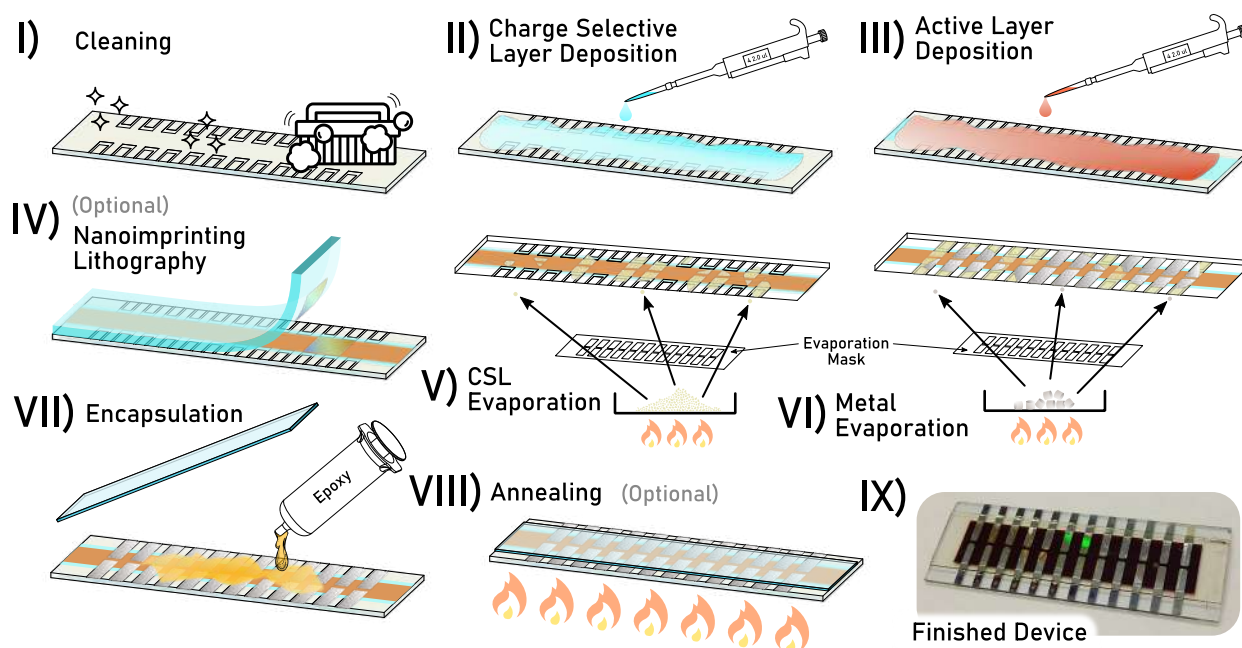


Figure 1.1: Full generic organic solar cell fabrication process with both required and optional steps clearly depicted in their chronological fabrication order.

1.1.1 Materials

Substrates

The substrates used throughout this thesis consist of a 1.1 mm thick glass slide, covered with a 100 nm **ITO layer** with a conductivity of $20 \Omega \square^{-1}$. Various different substrate sizes and distributions have been used to adapt experiments to our specific needs (Figure 1.2).

The biggest substrate has a rectangular shape (7.5 x 2.5 cm) ever so slightly smaller than most glass slides, and it is used as a **pre-scale up substrate** sourced from Ossila.¹ The ITO layer of this substrate is patterned (Figure 1.2 (Patterned ITO)), allowing us to manufacture 12 individual devices on each side of the slide, each one with an active area of 8 mm^2 , resulting in a total of 24 devices per substrate. We have taken advantage of this great number of devices to accelerate our research by changing various parameters (thickness, nanoimprinting depth, material...) within one single substrate, resulting in much lower material use and faster characterization times.

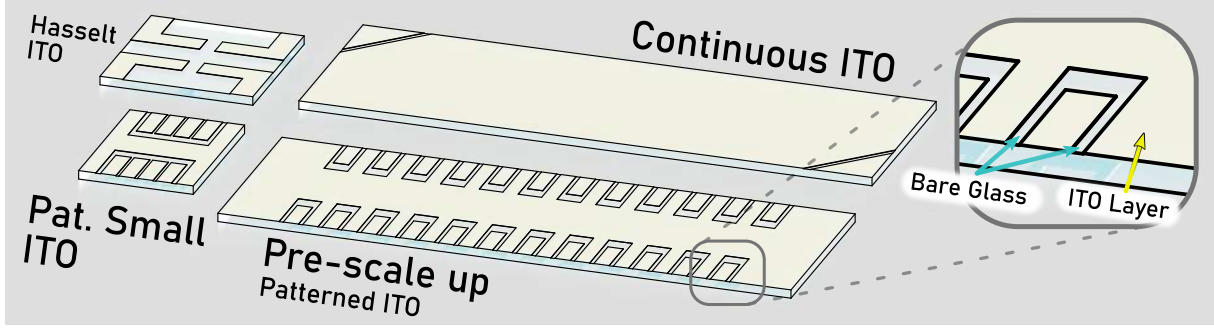


Figure 1.2: Different substrate types used throughout this thesis with their various ITO coverage patterns.

A slight variation on this substrate is the **continuous ITO** substrate, where the ITO layer covers the entire microscope slide homogeneously.² These substrates have been used to manufacture continuous electrode solar cells, mainly for photocurrent mapping purposes (Figure 1.2 (Continuous ITO)).

Besides these big substrates, we have also used smaller 8 pixel spin coater friendly substrates in multiple experiments.³ The main difference between these and the previous ones is their smaller pixel and substrate size, each pixel having an active area of 4 mm^2 , and lower amount of pixels per substrate (Figure 1.2 (Patterned Small ITO)).

Finally, we used an additional unconventional ITO patterned device that was specifically manufactured for the group of Koen Vandewal at Hasselt University. This substrates only had 4 pixels with an active area of 5.2 mm^2 (Figure 1.2 (Hasselt ITO)).

Electrode Materials

Front electrode transparent **ITO** substrate coatings were 100 nm thick with a conductivity of $20 \Omega \square^{-1}$ for the ones provided by Ossila¹⁻³ and a conductivity of $10\text{-}15 \Omega \square^{-1}$ for the ones provided by “BIOTAIN HONG KONG” to Hasselt University.

Back electrode materials include **silver** (Ag 99.99% shot) and **gold** (Au 99.999% shot) for inverted architectures, and **calcium** (Ca 99% 3 mm pieces) for conventional architectures, all thermally evaporated from pellets provided by Kurt J. Lesker.

Electron and hole transport layer Materials

In **inverted** solar cells:

Two different **zinc oxide** (ZnO) formulations have been used as ETL within this work: A **ZnO nanoparticle** dispersion (N-10 Avantama) in isopropanol (IPA) and a **ZnO sol-gel** solution, chemically synthesised in our group by using recipe described by Tiwari et al.⁴

The HTL was composed of thermally evaporated **molybdenum trioxide** (MoO_3 99.9995% powder) from Alfa Aesar.

In **conventional** solar cells:

The HTL was blade coated onto the substrates using a **PEDOT:PSS** solution purchased from Heraeus (CleviosTM - PEDOT:PSS P VP.AI 4083). The ETL was thermally evaporated onto the active layer using **lithium fluoride** (LiF) (99.85% (metals basis)) in powder form from Alfa Aesar.

Solvents

Every solvent used for blend solution preparation was purchased from Merk (Sigma Aldrich). Solvents were used as purchased, without any further purification. Used solvents were chlorobenzene (CB), o-dichlorobenzene (DCB), toluene and o-xylene (all being ACS reagent grade). Solvents used for cleaning purposes such as acetone, 2-propanol and ethanol were purchased from Labbox and were labeled as General Laboratory Reagent (GLR).

Active Layer Materials

The active layers fabricated during this thesis mainly consist of a blend between an electron acceptor material and an electron donor material. All active layer materials used in this work are commercially available, purchased from a variety of providers.

List of used materials:

- **Donors:**
 - - P3HT (Regioregular, electronic grade 99.995% $M_n = 30-60 \times 10^3$ (Merk))
 - - PBTTT (One Material Lot#YY7096)
 - - PBDB-T (One Material Lot#YY16128CH)
 - - PBDB-T-2Cl (One Material Lot#YY15156CH)
 - - PBDB-T-2F (One Material Lot#MY7206CH100)
 - - PTB7-Th (Ossila M_w 57183 Da)
- **Acceptors:**
 - - PC₆₁BM (Sigma Aldrich Lot#MKBK5229V)
 - - PC₇₁BM (Ossila >99%)
 - - ITIC (One Material Lot#DW3215)
 - - O-IDTBR (One Material Lot#DW4035P)
 - - Y6 (One Material Lot#DW6034P)
 - - ITIC-4F (One Material Lot#DW4108P)
 - - O-IDFBR (One Material Lot#YY12077)
 - - EH-IDTBR (One Material Lot#YY12076)
 - - IO-4Cl (One Material Lot#QL21061P)
 - - COTIC-4F (One Material Lot#DW7206P)

Specific solution preparation parameters, such as material concentration and ratio, varied significantly between experiments so they will be specified within each chapter. The only common step was to dissolve the materials in a solvent and stir them overnight at 80°C.

1.1.2 Cleaning

Every substrate used in this thesis was thoroughly cleaned before solar cell fabrication to ensure proper electrical contact and wettability. The substrates were cleaned by sequentially immersing them for 5 min in **ultrasonication baths** with different **cleaning solutions**, rinsing them with water in between baths to minimize bath contamination. The cleaning bath solutions were, in this order: acetone, 2% vol. Hellmanex solution in H₂O, isopropanol and 10% w/v NaOH in an aqueous solution. Finally, substrates were dried with compressed air.

As an additional step, some substrates were treated with **UV-ozone** for 20 min to further improve wettability. This whole cleaning procedure was optimized during this work, with several upgrades being designed and manufactured to enhance cleaning procedure performance.

1.1.3 Blade Coating Deposition

Blade coating deposition, is a solution deposition method widely used within research in the field of organic electronics in general, and specially in organic photovoltaics,^{5,6} **mainly because of its scale-up potential and because it is usually regarded as a previous step for large-scale manufacturing.**⁷ In this thesis, it has been used as the main manufacturing method for depositing most of the solution processed layers in a variety of OPV devices.

In Figure 1.3 we can see a simplified sketch that depicts the typical process in a schematic way. A droplet with a specific volume of **solution** is placed within the gap between the blade and the substrate, ideally wetting both and forming **meniscus** on either side of the blade. Afterwards, the blade is moved forward at a constant speed by a motor, and shear forces modify the liquid meniscus shape behind the blade. The blade motion evenly **distributes** the liquid along the substrate, with the liquid layer thickness being directly proportional to meniscus volume, which itself is proportional to blade speed. The drying process is mainly governed by the temperature of the substrate, placed on a regulable heated platform, and air currents around the substrate, which promote **evaporation**.

There have been several studies relating the resulting layer thickness with the various parameters involved during the blade coating process.^{8,9} However, from a practical point of view, blade gap,

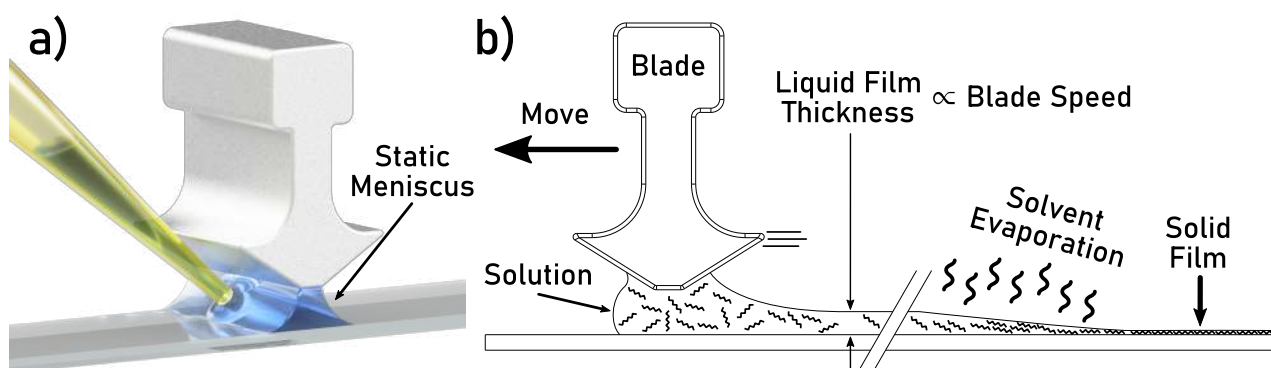


Figure 1.3: (a) Blade coating meniscus formation between blade and substrate after solution deposition. (b) Blade coating working principle, with liquid film formation, solvent evaporation and subsequent solid film formation.

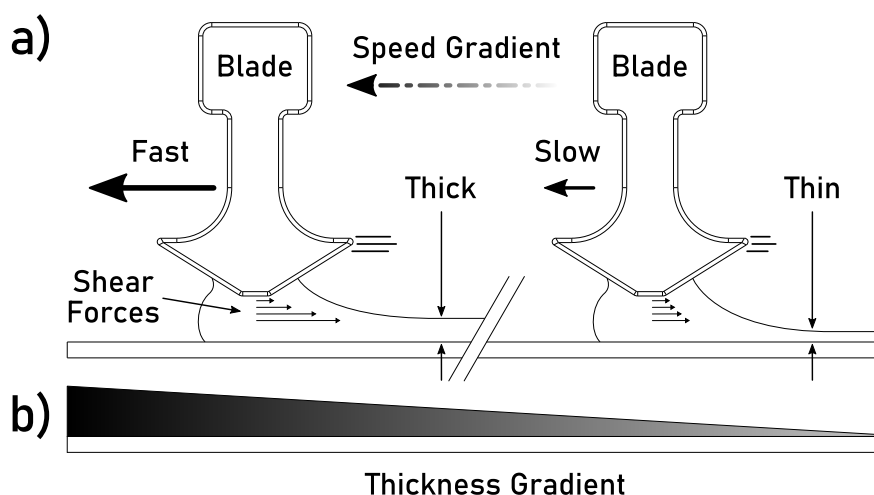


Figure 1.4: (a) Blade coating speed and liquid layer thickness relationship, related to the appearance of liquid shear forces between blade-liquid-substrate interaction. (b) Layer thickness gradient along a single substrate resulting from a controlled speed gradient during blade coating deposition.

cast volume and **blade speed** usually have the most significant effect on final **film thickness**, the latter being the one with the strongest influence.

Since blade speed is one of the main parameters used to control layer thickness, in our group Dr. Bernhard Dörfling modified a commercial blade coater unit (ZUA 2000, Zehntner) by connecting its motor controller to an Arduino, so that the blade coating motor can vary operating speeds and accelerations within one single deposition. This **variable blade speed** allows us to deposit layers with a **thickness gradient**, by changing the speed of the blade during deposition, as can be seen in Figure 1.4. Within this work, most thickness gradient active layer films were cast by decelerating the blade from $99 \text{ mm} \cdot \text{s}^{-1}$ to $1 \text{ mm} \cdot \text{s}^{-1}$, during the deposition across the entire substrate length (75 mm), to provide the widest possible thickness range.

This variable speed approach enables the characterization of material thickness dependent performance in a single substrate. Such a strategy can be applied to a wide variety of solution-processed layers, but in this thesis it has been mainly applied to photoactive **layer optimization**. In most active layers manufactured using this approach, typical thickness gradients ranged anywhere from 300 to 50 nm. Nonetheless, the exact film gradient thickness is determined by the specific solution processing parameters and the choice of donor/acceptor materials.

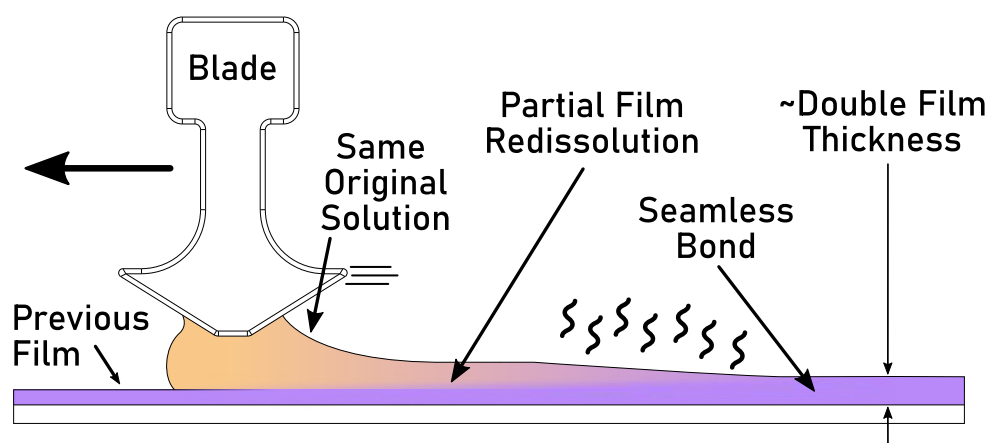


Figure 1.5: Subsequent layer deposition using the same solution for the original bottom film and the new overlaid film. The partial film redissolution aids in the formation of a seamless bond resulting in an almost twice as thick film.

The reproducibility of such accelerated blade coating deposition was confirmed by our colleague Dr. Enrique Pascual. By fabricating three batches of P3HT:O-IDTBR devices with the same processing conditions on different days, he demonstrated a consistent deposition thicknesses within 5% of standard deviation, confirming the **reproducibility** of this novel blade deposition method.¹⁰

One of the caveats of regular blade coating deposition is that, for typical solubility-limited solution concentrations used in OPV, the thickness range is somewhat limited on the higher end, where the deposition of several μm thick films remains challenging. In this work we have developed a rather simple approach to tackle this problem where, by depositing a series of **subsequent layers**, we are able to fabricate very **thick homogeneous films** (Figure 1.5). The method relies on the speed relation between film dissolution and solvent evaporation. By blade coating a material solution on top of a dry layer made from the exact same material, if the solution is concentrated enough and the substrate is hot enough, the solvent will evaporate before the dry layer has time to fully dissolve, resulting in an effective stacking of the two films with a **seamless bond** with good electrical properties and no layer separation. In this way, we are able to stack several films on top of each other, achieving layers with ever increasing thickness. In this work we have manufactured devices of up to 8 times the maximum thickness of a single deposition.

The main drawback of this technique is that each subsequent film has small imperfections that can stack up, so after many depositions film homogeneity can be compromised. Another small inconvenience is that any gradient generated by uneven deposition can be exaggerated after subsequent film depositions. However, this can be easily mitigated by rotating the substrate by 180 degrees after each deposition. Doing so prevents strong gradients from forming, while evening out small unintentional gradients that might have formed during deposition.

1.1.4 Spin Coating Deposition

Spin coating deposition is a thin film coating technique that produces thin homogeneous films with a high degree of control and reproducibility, making it the most used deposition technique in the field of OPV.⁵ In this thesis, this technique has been used to manufacture a limited number of devices, mainly those manufactured during my stage in Hasselt University, where blade coating was not the main manufacturing method, encompassing the work of Chapters ?? and ??.

This technique is based on depositing a viscous fluid on a **horizontal rotating surface**, where the rotating motion ejects most of the solution leaving a thin and uniform liquid layer. The working solution is usually composed of a solute and a solvent, which gradually evaporates leaving the solute behind and forming an equally **uniform solid film** (Figure 1.6).

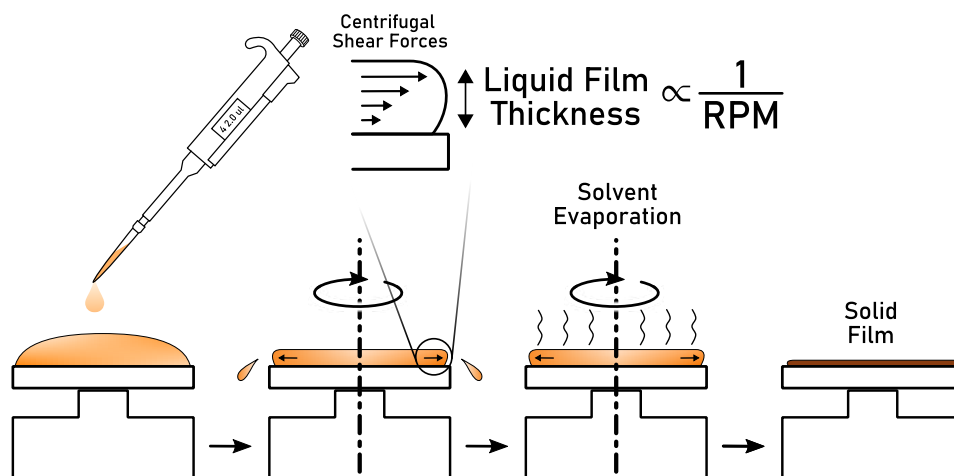


Figure 1.6: Spin coating working principle depicting the major steps in the process with the active layer thickness and rotational speed relationship through liquid shear forces.

Common practice dictates that liquid deposition should be performed with the substrate being static or rotating at low angular velocities, a practice we call static deposition. After the liquid has covered the entire substrate, the latter is rapidly accelerated to a high angular velocity (spin speed). The adhesive forces at the liquid/substrate interface and the **centrifugal forces** acting on the rotating liquid result in strong sheering forces on the liquid layer, causing a radial flow in which most of the deposited solution is rapidly ejected from the substrate. Eventually these two forces equilibrate, resulting in a **thin liquid film**, with a highly homogeneous thickness over the entire substrate. This film is kept at a constant spinning speed to maintain film thickness during **solvent evaporation**, until a solid solute film is formed, with practically no solvent left. A variant of this process, commonly used for low vapour pressure solvents, consists on depositing the solution while the substrate is already spinning, a practice commonly referred to as dynamic deposition.

Over the last several decades a great deal of experimental work has been performed trying to deduce empirical correlations between experimental parameters and film thickness.^{11–15} The results from these studies indicate that **angular velocity**, solution viscosity and **solution concentration** are the main driving factors determining final **film thickness**. On the other hand, the amount of solution initially deposited on the substrate, solution deposition rate, the history of rotational acceleration prior to final acceleration, and the total spin time have been seen to have limited to no effect.¹¹

The generalized correlation between spin coating parameters and film thickness can be described by the following, empirically derived, formula:¹¹

$$h = k_2 \eta_0^\beta \omega^\alpha \quad (1.1)$$

Where **h** is the film thickness, η_0 is the viscosity of the deposited solution, ω is the angular velocity, α and β are empirically found exponents and k_2 is an empirically calculated constant that is strongly related to the specific solute/solvent blend.

In a polymer solution, liquid viscosity increases at higher concentrations in a non linear manner. As a result, higher concentration solutions will lead to thicker films when spin coating at similar speeds. However, the easiest way to modify film thickness without needing to change processing parameters is to modify the angular substrate velocity, which is directly proportional to the centrifugal force. By tuning the shear force equilibrium, one can accurately control the liquid film thickness, which is directly proportional to final solid film thickness. As we can see in Figure 1.6, higher rotational speeds lead to thinner films, due to higher shear forces on the deposited liquid.

1.1.5 Thermal Evaporation

Thermal evaporation is a physical deposition technique employed in thin film deposition for multiple layers in organic photovoltaics.¹⁶ In this thesis, this process has been used to deposit the metallic back electrode as well as the charge selective layer on top of the active layer.

The process of thermal evaporation consists on the evaporation of a coating material by raising its temperature in a high vacuum.¹⁷ In the case of metals and oxides, such as the ones used in this work, this process requires the evaporation material to be at extreme temperatures in the range of 1000°C, and really high vacuum levels of around 10^{-4} Pa, due to their extremely low vapour pressures caused by strong atomic and molecular bonds.

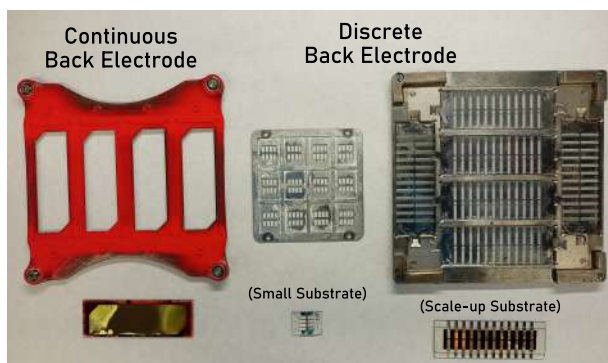


Figure 1.7: Evaporation masks for different electrode type manufacturing, with the resulting evaporated electrodes on different devices (bottom).

In order to achieve such high vacuum levels a combination of a mechanical and a turbo-molecular pump are used, which are capable of maintaining stable vacuum levels of vacuum along the deposition process, pumping out any adsorbed gas released during the evaporation.

Maintaining a stable vacuum is crucial for proper layer deposition, because a slight rise in pressure levels can completely stall the evaporation process.

Thermal evaporation was used to subsequently deposit the MoO_3 HTL and the Ag back electrode, at a rate of 0.05 nm s^{-1} and 0.1 nm s^{-1} respectively, through a series of custom designed shadow masks to produce different electrode distributions depending on the specific substrate ITO pattern (Figure 1.7). The evaporation rate for LiF was lower at 0.01 nm s^{-1} . The thermal evaporator used was a ECOVap from MBraun attached to a nitrogen glovebox, and the layer thickness was measured using a quartz balance crystal. All depositions were performed under high vacuum conditions of $8 \times 10^{-5} \text{ Pa}$.

1.1.6 Encapsulation

In order to **prevent** oxygen and moisture driven **degradation**, in this thesis most devices were **encapsulated** by using a UV curable **epoxy resin** and a glass coverslip that acted as a physical barrier for ambient oxygen and humidity. In this way, device lifetime was significantly extended, enabling us to perform longer measurements without excessive degradation. After encapsulation, the most important remaining degradation driving factor was light.

Ideally, the used epoxy resin should not interact or affect the finished device in any way. However, general device performance is lower after encapsulation, a fact that we attribute to partial active layer blend dissolution during encapsulation, with some of the active layer components being soluble in the uncured liquid epoxy resin. Even though the active layer is mostly protected by the silver back electrode, epoxy resin can dissolve the uncovered regions surrounding the electrode, partially leeching into the solar cell active layer and hindering device performance.

In order to increase the reproducibility of the encapsulation process we designed small guides to align the substrate with the coverslip, greatly increasing device consistency, and allowing for the systematic measurement of encapsulated devices in the measurement setups discussed in following Chapters.

The epoxy was sourced from DELO, and the type is KATIOBOND LP655. The encapsulation slides were 0.5 mm glass cover slips sourced from Ossila.¹⁸

1.1.7 Thermal Annealing

One of the most important properties of organic electronic devices is the **morphology** of the organic layers. Polymers used in such layers consist of long chain molecules **they** can exhibit a wide variety of crystalline phases, as well as a varying degree of **crystallinity**. Organic photoactive layers usually consist of two different materials, a polymer and small molecule, which lead to a wide variety of possible crystalline states and phase segregation conditions.

Maybe the easiest approach to control these conditions in order to optimize blend morphology, is to subject organic layers to a **thermal annealing** process. This process consists on raising and lowering the layer's **temperature** in controlled steps, navigating the phase diagram in the process and modifying blend **crystalline properties**.

In this thesis, there have been a limited number of studies focused on the effect of the annealing process on active layer morphology, further described in Chapters ?? and ??. For thermally annealed devices, the process was carried out with a single temperature step, heating up to a certain temperature and then cooling down to room temperature, on a homogeneous temperature hotplate (SD162, Stuart), performed inside of the glovebox.

1.2 Nanoimprinting Lithography

Nanoimprinting lithography is based on the more general process known as lithography, which can be generally described as a process to transfer superficial features on a mould onto any desired substrate (Figure 1.8). In this thesis, we have focused on nanoimprinting soft lithography to nanostructure the active layer of organic solar cells and organic photodetectors with the shape of a photonic crystal, in order to enhance their absorption and performance, as further described in Chapter ??.

This process consists on **transferring** the superficial **features** of a mould, or **stamp**, onto a **substrate** of interest, usually resulting in a negative impression of the mould shape on the

surface.¹⁹ Feature transfer is usually achieved by placing the mould over the substrate when its material resistance to plastic deformation is low. There are **multiple strategies** to lower this resistance, such as heating the substrate up to the melting point, or **heating it up to the** glass transition and applying pressure on the mold, or even using a solvent to dissolve the substrate surface before placing the mould, and waiting for the solvent to evaporate leaving the solute with the exact mould shape.

Over the last decades, this process has been refined up to the point where **nanometric features** (20-2500 nm) can be easily obtained with high fidelity and reproducibility.²⁰ Its main advantages include mold reusability, ambient processing conditions, wide area coverage, roll-to-roll compatibility, material independence, and the fact that the smallest possible features are not diffraction limited, resulting in significantly lower operation and maintenance costs when compared with traditional lithography techniques.¹⁹ Because of all these advantages, NIL has been gaining popularity in recent years, being used in fields outside conventional semiconductor industry, such as flexible organic electronics, biocompatible materials and other experimental materials, with a variety of applications, from solar cells and metamaterials to nanofluidics and nanoelectronics.²¹⁻²⁴

1.2.1 Thermal Nanoimprinting Lithography

Thermal nanoimprinting lithography consists on transferring mould features onto a **thermo-plastic** substrate, by pressing it against a temperature resistant mould, while **heating** it above its glass transition temperature, or above its melting point, to significantly reduce its storage modulus, making plastic deformation the main deformation mechanism.¹⁹ In this way, all the mechanical energy imparted on the substrate material will result in a non-elastic, **permanent deformation**. Because of its application simplicity, in this thesis this procedure has been used to nanostructure the active layer of most devices.

The entire process consists of just three simple steps: Place the mould on top of the substrate, apply **pressure** while performing a full temperature cycle, up and down, and carefully release the

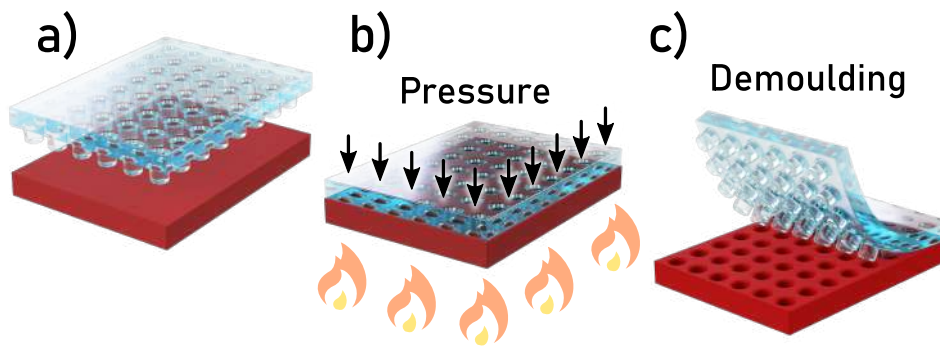


Figure 1.9: Thermally assisted nanoimprinting lithography depicting the three very basic steps involved in the process: (a) nanostructured stamp approximation, (b) combined pressure and heat for layer plastic deformation, and (c) careful demoulding.

mould (Figure 1.9). The last step being the most critical, where the mould needs to be carefully removed with a soft continuous motion to prevent damaging the newly created nanostructures. A rapid or discontinuous **demoulding** leads to inconsistencies and defects on the nanostructures. The negative features of the mould can be immediately seen along the substrate surface after demoulding usually as an iridescent pattern (Figure 1.8).

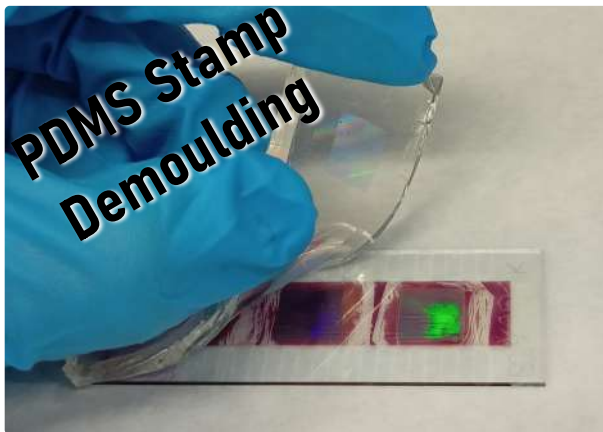


Figure 1.8: Iridescent pattern characteristic of nanostructured surfaces using lattice parameters on the same order of magnitude than visible light wavelengths. This iridescent pattern indicates the successful transfer of stamp features into the organic layer.

The applied pressure will depend on material viscosity, where the weight of the mould itself is enough to transfer the features for the lowest viscosity materials, while for high viscosity materials a huge amount of force is necessary for proper feature transfer. This technique is not suitable for materials that degrade at temperatures lower than their glass transition temperature or their melting point, mainly because of the inability to lower their storage modulus enough for correct feature transfer.

In this thesis, most thermal assisted nanoimprinting lithography was performed at 5×10^5 Pa, with various temperature cycles going on the way up to 200°C .

1.2.2 Solvent Assisted Nanoimprinting Lithography



Solvent assisted nanoimprinting lithography is another **variant of NIL** that relies on the use of **solvents** to assist with **feature transfer** between mould and substrate. This process takes advantage of the chemical interactions between a solvent and the substrate material to temporally **reduce its elasticity, promoting a plastic behaviour**. Proper solvent removal is necessary before demoulding to prevent the nanostructures from disappearing after mould release. In this thesis, this process has been used in active layer nanostructuring, immediately after layer solution processing, before the solvent has had time to fully evaporate.



The process begins by exposing the substrate material to a solvent, either by directly dropping solvent onto the substrate, by exposing the substrate to solvent vapour, by wetting the mould itself, or by placing the mould onto the freshly deposited layer after solution processing. The solvent weakens the material molecular bonds and as a result the material transitions into a more **malleable phase** where, by pressing a nanostructured mould onto the substrate, the mould's features can be accurately transferred. The pressure needs to be maintained until the solvent is completely evaporated, in order for the substrate to regain its original stiffness. **Solvent evaporation** can be assisted with artificial heating and or forced air flow, after which the mould can be slowly and carefully removed to reveal the nanostructured substrate surface.

This NIL procedure is highly compatible with roll-to-roll solution processing techniques, where it can be implemented immediately after solution layer deposition, before the layer is completely dry. In this thesis, most solvent assisted NIL has been performed immediately after blade coating, on freshly deposited partially wet layers. **In order to enhance the reproducibility of this technique, we developed a small accessory guide, for the moulds to be precisely located during the nanostructuring.**

1.2.3 Stamp Fabrication and Architecture

The nanostructuring moulds, or stamps, used throughout this thesis are made with a curable **polymer resist** called **Polydimethylsiloxane** (PDMS), used because of its variable stiffness properties, chemical inertness, and really **good feature reproduction fidelity**. All stamps are exact reproductions of a “Master Stamp”; a **high precision** nanostructured silicon wafer that is fabricated using interference lithography. The reproduction procedure consists of several replication steps, using different materials to reduce the interaction with the delicate “Master Stamp”.

The process begins with master stamp silanization, covering the silicon with a single molecule thick layer of perfluorooctyl-trichlorosilane, which acts as a release agent, preventing the silicone based replica from covalently bonding to the master. To make sure this layer is as thin as possible, after exposing the master to a vapour of perfluorooctyl-trichlorosilane, we rinse it with acetone and **heat it up to 150°C** to remove the excess compound. **We replicate the silanized using a thin layer of UV curable OrmoStamp® resist, which after cured over a glass substrate, following the preparation instructions, serves as a high resistance intermediate stamp for further reproduction.**²⁵ **This photocurable polymer resist has a really high young modulus (650 MPa), suitable for replicating fine structures with high aspect ratio and with excellent mechanical stability, but excessively stiff and brittle for repeated use with thermal NIL.**

These OrmoStamp® masters are then replicated with a “**hybrid mould**” PDMS architecture, which consists on a **combination** of a thin layer of **high stiffness** (hard) PDMS, and a thick layer of **low stiffness** (soft) PDMS (Figure 1.10). This architecture, developed **within our group**, takes advantage of the high stiffness of hard PDMS, to accurately replicate the nanostructures onto hard materials, and the conformality and deformation of soft PDMS, to ensure an intimate contact between stamp and substrate during the process, and to act as a backbone for the

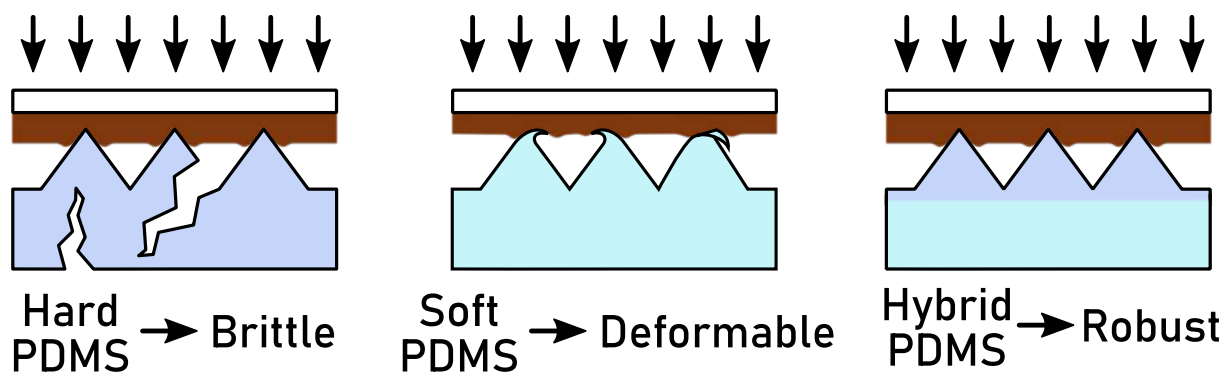


Figure 1.10: Different PDMS type stamps: Hard PDMS, which is brittle but can penetrate without problem into most active layers, even those with a high young modulus. Soft PDMS, which is really resistant to breakage but can be easily deformed by materials with high young modulus. Hybrid PDMS, which combines the best of both worlds, with a high young modulus thin layer of hard PDMS and a robust thick layer of soft PDMS that serves as a backbone.

brittle hard PDMS, limiting crack formation and stamp degradation with use. Being made from exactly the same material, the two different layers form a seamless bond, effectively becoming one single piece, even though they are manufactured in two separate steps.

Hybrid **M**oulds are prepared in two steps: first we mix the ingredients for hard PDMS, which are vinylmethylosiloxane and hydroxyl siloxane, the polymer precursors, Platinum(0)-1,3-divinyl-1,1,3,3-tetramethyldisiloxane, the catalyst to cure the resin, 2,4,6,8-tetramethylcyclotetrasiloxane a reaction modulator, and some toluene to lower the mixture viscosity and assure proper feature reproduction. The resulting liquid is carefully poured over the silanized OrmoStamp® master, forming a thin bubble free layer that is cured at 60°C for one hour. While this is curing we prepare the soft PDMS backbone by mixing SYLGARD 184 elastomer base with its curing agent in a 10:1 ratio, thoroughly degassing the mixture. Once the hard PDMS is cured, we pour the soft PDMS mixture on top completely covering the OrmoStamp® master, and we set it to cure at 60°C for 3 hours in the oven. After the soft PDMS is completely cured, the OrmoStamp® master is carefully demoulded from the hard PDMS, leaving behind a solid stack of thin hard PDMS on the top and thick soft PDMS on the bottom, which can already be used as a nanostructuring stamp.

1.2.4 Stamp Feature Depth

The described fabrication method allows us to obtain nanostructured stamps with a variety of lattice parameters, determined by the silicon master, with a constant feature depth of around 300 nm. In this thesis, however, we required different **nanostructuring depths**, as further explained in Chapter ??, so my colleague Dr. Molet developed and optimized a reproducible process that uses **reactive ion etching** to obtain stamps with **variable feature depth**.

This process consisted on transferring the desired features back onto a silicon substrate, by covering it with a thin layer of photocurable resin (SU-8) and nanostructuring said layer with a soft PDMS stamp with the desired features. After curing the resin, the silicon substrate was etched for different amounts of time using reactive ion etching, a highly directional etching technique, resulting in new “silicon master” moulds. These silicon masters had the same nanostructure lattice parameters as the soft PDMS, but a variety of **feature depths**, proportional to **etching time**. These were used to fabricate new shallow nanostructure PDMS stamps, used to nanostructure the polymer layer blends used in Chapter ??.

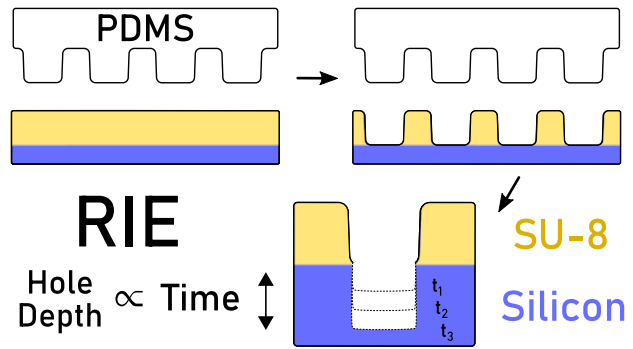


Figure 1.11: Variable depth master mould fabrication with SU-8 layer on silicon substrate acting as a nanostructured mask. SU-8 covered regions are not affected by RIE, while exposed silicon regions are etched in proportion to etching time, resulting in different depth nanostructures.

1.3 Device Characterization

In order to assess the performance and fundamental characteristics of our devices, a variety of characterization techniques have been used throughout this thesis. The main purpose of this section is to very briefly describe the working principle of the different techniques, and to specify the equipment used in each measurement. They are arbitrarily separated between

electrical characterization, where we majoritarilly evaluate device performance and electrical characteristics, and optical and topological characterization, where we evaluate mostly device morphology and its light interaction characteristics.

1.3.1 Electrical Characterization

The main techniques used to electrically characterize our devices are JV-Curves, which measure current density of our device at different voltages; External Quantum Efficiency (EQE) curves, which measure the efficiency of our devices at converting incoming photons into electrons; Light Beam Induced photoCurrent (LBIC) maps, where we can evaluate the local performance of a solar cell at several positions creating an effective efficiency map; and Transient Photodiode Response, where we evaluate photodiode speed performance.

JV Characterization

In our lab, **JV curves** have been measured using a custom made semi-professional JV characterization setup, consisting of a demultiplexing board in combination with a LabVIEW application, which have been fully developed **under the umbrella of this work** (further described in Chapter ??). This setup is connected to a **Keithley 2400 source meter** that performs the high precision current and voltage measurements. In order to illuminate our devices, we have used a **solar simulator** (XES-100S, SAN-EI Electric) under **AM 1.5G** (Air Mass 1.5 Global) and 1000 W m^{-2} illumination. Being AAA class, this solar simulator guarantees a homogeneous illumination area of $10 \times 10 \text{ cm}$, which has proven to be extremely useful to characterize all our different devices, which measure up to 7.5 cm long. The solar simulator was calibrated before each experiment to ensure the measurement reliability, using a certified reference silicon solar cell (Oriel, Newport).

In this thesis, JV curve measurements have been one of the main performance characterization methods, being widely used in every chapter.

External Quantum Efficiency

External quantum efficiency measurements have been performed on a custom made semi-automated experimental setup, with an associated LabVIEW controlling Software, fully developed under the umbrella of this thesis (further described in Chapter ??). This experimental setup is coupled to a **supercontinuum laser** light source and a computer-controlled **monochromator** (LLTF contrast, Fianium), which is further filtered to provide a continuous spectral range. With this setup we are able to illuminate the sample with light ranging from 400 nm to 1100 nm, range which can be further extended into the infrared by changing the monochromator. The current measurements were performed with a Keithley source meter 2450.

EQE measurements have been the other main performance characterization method used throughout this thesis, which have been combined with JV measurements to assess solar cell and photodetector efficiency in every chapter.

LBIC Maps

Light Beam Induced photoCurrent (LBIC) maps are a really useful tool to assess the **localized performance** of optoelectronic devices. To obtain such maps, the optoelectronic device is illuminated with a concentrated **light spot**, around 50 μm in our case, that is **swept** over the whole sample, while measuring the generated **photocurrent** on each point.

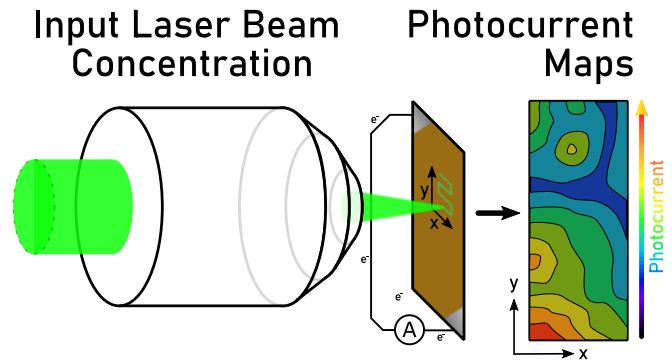


Figure 1.12: Light Beam Induced photoCurrent Map generation by scanning a laser beam focused with a microscope objective throughout a sample, while recording the photocurrent at each point.

In this way we obtain a photocurrent map of our entire device that shows light power conversion efficiency distribution along the entire photoactive layer (Figure 1.12). This procedure is usually performed using either monochromatic or white light. However, in this work, we have modified an existing setup, connecting it to the supercontinuum/monochromator source, so that we can

illuminate the sample with any desired wavelength. As a result, we have been able to measure the performance distribution of various devices at very different wavelengths, as can be seen on Chapter ??.

LBIC measurements were performed using an experimental setup assembled within our group, mainly consisting of parts bought from Thorlabs. As stated before, the illumination source was the supercontinuum laser light source and a computer-controlled monochromator (LLTF contrast, Fianium), while the sample was moved using Thorlabs motors (25 mm (0.98") Low-Profile Motorized Translation Stage) and the current was measured using a Keithley Source Meter 2400. The entire setup was controlled using custom made LabVIEW scripts developed within our group.

Transient Photodiode Response

In order to characterize **transient photodiode response**, which can be seen in Chapter ??, we slightly modified the existing EQE setup by placing a **mechanical chopper** in the laser light path, which temporally interrupted the photodiode illumination, allowing for an easy control of both illumination rate and wavelength. To characterize such fast responses we used an Teledyne Lecroy WP804HD brand **oscilloscope**, which measured the voltage drop on a $50\ \Omega$ resistor connected across the leads of the device being characterized.

1.3.2 Optical Characterization

Fourier Transform Infrared spectroscopy (FTIR)

Fourier Transform Infrared spectroscopy (FTIR) is a fast and reliable way to obtain the absorption spectra of a sample. This spectroscopic technique differs significantly from the more conventional “dispersive spectroscopy”, where the sample is illuminated by one wavelength at a time, and we measure how much light is absorbed at each wavelength over a defined range. The main advantage of FTIR spectroscopy is that we shine the sample with light

containing **multiple wavelengths** and we measure how much light is **absorbed**. After the first absorption measurement, the instrument changes the **wavelength combination** of the incoming beam and repeats the absorption measurement.¹ This process is rapidly repeated many times over a short time span, while a computer takes the resulting interferogram and, by applying a **Fourier Transform**, it calculates the absorption of the sample at each wavelength. The various wavelength combinations used in this technique are the result of a combination between a broadband light source, which covers the entire spectrum to be measured, and a Michelson interferometer.

To perform most of the absorption spectra obtained throughout this thesis, we measured both transmission and reflection spectra using a Bruker Vertex 70 FTIR spectrophotometer attached to an optical microscope (Bruker Hyperion). The microscope allowed us to accurately position the sample within the measuring spot. The spectra were recorded using a 4x objective with numerical aperture (NA) of 0.1, for both emission and collection, having a spot size of $400\text{ }\mu\text{m}^2$. The wavelength range of every measurement was from 400 nm to 1100 nm. Reflectance measurements were normalized against calibration silver and **gold mirrors**,² for visible and **infrared ranges** respectively, and a clean glass slide for the transmission measurements.

Integrating Sphere Spectra

An **integrating sphere** is an optical device used to quickly and reliably measure reflectance and transmittance spectra.³ This element consist of a hollow highly **diffusive** sphere, with lateral holes used as input and output ports, which scatters incoming light to remove spectral directionality components. There are two main measuring modes: **Transmittance**, where the sample is placed on the light input port, filtering incoming photons, with every other port plugged with highly diffusive plugs, which results in a transmission spectrum; and **Reflectance**, where the sample substitutes one of the output ports, reflecting only a certain photon fraction, resulting in a reflection spectrum. The reflection spectrum is normalized to that of a highly diffusive white material, which is considered to be 100% reflective, while the transmission spectrum can be normalized with any material, such as a glass substrate, by first measuring its transmittance

and then using it as the background signal. This characterization method allowed us to measure the reflectance and transmittance spectra of several active layers of organic solar cells discussed in Chapter ??.

In order to perform the integrating sphere measurements, we used an ISP-REF Integrating Sphere coupled with a tungsten-halogen light source and a Flame spectrometer (Ocena Optics) through two optic fiber cables, all being controlled with the spectroscopy software OceanView.

1.3.3 Topological Characterization

To study the surface and thickness of our devices we decided to use two of the most commonly used techniques in material sciences, Scanning Electron Microscopy and Profilometry. These techniques give us insight on the surface topography, the layer thicknesses and the coating conformality of our devices among other information. Besides, Dr. Edgar Gutiérrez Fernández and Dr. Jaime Martín (Polymat) have performed both GIWAXS and GISAXS on some of our samples, characterize active layer blend morphology.

Scanning Electron Microscopy

Scanning Electron Microscopy (SEM) is a really powerful technique that provides close to **nanometric resolution** of a sample surface topology. This technique is based on **accelerating electrons**, collimating them into a beam, and focusing the beam onto a sample of interest. These accelerated electrons will interact with the sample in different ways, depending on the angle between the beam and the sample and its composition. By using different kinds of detectors, we can extract information about these interactions, and construct different images that provide **topology** and **compositional** information about the sample.

In Chapter ??, SEM has been extensively used to analyse nanostructure topology and to assess the conformality of the different layers on our devices. We have used a Quanta FEI 200 FEG-ESEM 53 electron microscope. For metal coated, or fairly conductive substrates, we have used the high vacuum mode (10^{-3} Pa) and voltages ranging from 10 to 15 KV. In the case of

poorly conductive substrates, such as PDMS, low vacuum conditions with a 60 Pa water vapor atmosphere and voltages from 5 to 10 KV were used, to minimize the aberrations caused by surface charge build-up.

Contact Profilometry

Contact profilometry is another useful technique that provides information about surface topology with a really high resolution. The main working principle is not that different from a record player, where a needle is gently moved in close contact over a substrate surface, with a very small contact force, causing the needle to be deflected by any change in **surface topology** as it moves through the substrate. This needle deflection is then transduced into an electrical signal, which can be directly related to the relative height of the sample along the needle's path. This technique is able to scan features with almost **nanometric vertical resolution** and sub-micrometric lateral resolution.

In this work we have mainly used profilometry to determine the thickness of the various layers within our device. The easiest way to determine **layer thickness** is by extracting a profile cross section through a step in the layer, which we artificially create by either depositing layers with a gap on the deposited material, or

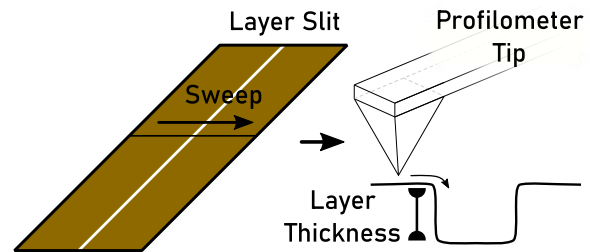


Figure 1.13: Profilometry layer thickness measurement, using a slit inscribed on the center of the layer, through which the fine tip of a profilometer is swept in order to measure the layer thickness.

by sharply scribing a gap (Figure 1.13), resulting in a slit on the layer to be measured. The equipment used was a KLA Tencor D-500 profilometer. Measurements have been performed with a diamond tip, placed in contact with the substrate applying a 0.03 mg contact force, and slowly scanning the sample at 0.1 mm s^{-1} along a specified line. This technique has been extensively used throughout Chapter ?? and ??, to relate deposition conditions with final layer thickness, and to perform correlation studies between active layer thickness and final optoelectronic device performance.

Grazing Incidence X-Ray Scattering Characterization

Grazing incidence X-ray Scattering is a characterization technique that consists on shining an X-ray beam onto a substrate at a very **low incoming angle** (grazing incidence) to limit light scattering to the superficial regions, making this technique highly **surface sensitive**. By operating close to the film critical angle, the evanescent wave established on the film decreases fast enough to guarantee that the signal is only coming from the topmost layer, with a penetration depth on the order of nanometers. That is why this technique is widely used in **thin film morphology** characterization. The main limitation of this technique is that, by projecting the beam onto the surface at really low angles, even relatively collimated beams exhibit wide beam footprints, limiting local resolution. As an example a $50\ \mu\text{m}$ beam at 0.1° incidence has a beam footprint of 28.6 mm, a spot 573 times bigger than the original.

This technique is further subdivided in **Grazing Incidence Wide Angle X-ray Scattering** (GIWAXS) and **Grazing Incidence Small Angle X-ray Scattering** (GISAXS), where their main difference is the **angle of diffracted light** captured by the detector. There is no universally accepted border between these two regimes, but in general GIWAXS focuses on detecting the entire scattering angular range by placing the detector close to the sample, while GISAXS is

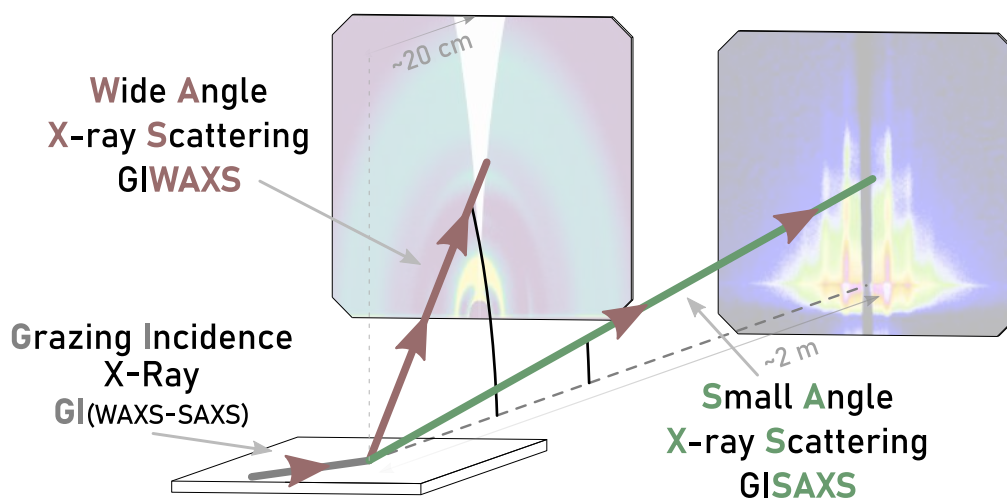


Figure 1.14: Basic detector sample distance relationship difference in GIWAXS and GISAXS.

centered around detecting the weakly scattered X-rays, with the detector far away from the sample.²⁶ The main difference between these techniques is the length scale they are probing, where **GISAXS** is used on determining **long range order** in morphology, with smaller diffraction angles, and **GIWAXS** being more involved in probing **atomic and molecular distances** in crystal lattices.

In this thesis, both GIWAXS and GISAXS have been used to characterize temperature dependent active layer morphology of devices manufactured in Chapter ???. The measurements, data processing and interpretation was fully performed by Dr. Edgar Gutiérrez Fernández and Dr. Jaime Martín.

GIWAXS experiments were carried out at NCD-SWEET beamline at **ALBA Synchrotron** (Barcelona). The samples were measured in a grazing-incidence geometry, placing the beam at an incident angle of 0.12° to probe the total volume of the film. The energy of the beam was 12.4 keV ($\lambda = 0.1$ nm) with exposure times of 1 s. The patterns were taken with the WAXS LX255-HS detector (Rayonix), placed at 20 cm from the sample position, using pixels of $88.5 \times 88.5 \mu\text{m}^2$. The 2D pixel maps were transformed into q-space and integrated using a self-made MATLAB script and pyFAI package of Python.

More info: <https://www.cells.es/en/beamlines/bl11-ncd>

GISAXS measurements were performed at SAXS beamline, at **Elettra Sincrotrone** (Trieste, Italy). Thin film samples were measured using an incoming X-ray beam at an incident angle between 0.12° and 0.15° and exposition times of 10 s. The wavelength of the X-ray beam was $\lambda = 0.154$ nm ($E = 8$ keV). The patterns were taken using a Pilatus 1M detectors (Dectris), with a pixel size of $172 \times 172 \mu\text{m}^2$, placed at 1200 mm from the sample. 2D pixel maps were transformed into q-space and integrated using a self-made MATLAB script.

List of Tables

List of Figures

1.1	OPV fabrication process	3
1.2	Substrate types	4
1.3	Blade coating working principle	7
1.4	Blade coating thickness variation	8
1.5	Subsequent blade coating deposition	9
1.6	Spin coating working principle	10
1.7	Evaporation masks for different electrodes	12
1.9	Thermally assisted nanoimprinting lithography	16
1.8	Nanostructure iridescent pattern	16
1.10	Different PDMS type stamps	19
1.11	Variable depth master mould fabrication	20
1.12	Light Beam Induced photoCurrent Maps	22
1.13	Profilometry layer thickness measurement	26
1.14	GIWAXS and GISAXS detector distribution	27

- ¹, Ossila. ITO Glass Substrates | PV and OLED, 75 x 25 mm | Ossila.
- ², Ossila. ITO Glass Substrates, Unpatterned 75 x 25 mm | Pack of 100 | Ossila.
- ³, Ossila. ITO Glass Substrates | PV and OLED, 20 x 15 mm | Ossila.
- ⁴, D. C. Tiwari, S. K. Dwivedi, P. Dipak, T. Chandel, and R. Sharma. Sol-gel derived ZnO as an electron transport layer (ETL) for inverted organic solar cells. In *AIP Conference Proceedings*, volume 1832, page 060024. American Institute of Physics Inc., 5 2017.
- ⁵, P. G. V. Sampaio, M. O. A. González, P. Oliveira Ferreira, P. Cunha Jácome Vidal, J. P. P. Pereira, H. R. Ferreira, and P. C. Oprime. Overview of printing and coating techniques in the production of organic photovoltaic cells. *International Journal of Energy Research*, 44(13):9912–9931, 10 2020.
- ⁶, G. Bernardo, T. Lopes, D. G. Lidzey, and A. Mendes. Progress in Upscaling Organic Photovoltaic Devices. *Advanced Energy Materials*, 11(23):2100342, 6 2021.
- ⁷, J. Cheng, F. Liu, Z. Tang, and Y. Li. Scalable Blade Coating: A Technique Accelerating the Commercialization of Perovskite-Based Photovoltaics. *Energy Technology*, 9(8):2100204, 8 2021.
- ⁸, M. Sajid, M. Mughees, N. Ali, and H. Shahzad. A theoretical analysis of blade coating for third-grade fluid. *Journal of Plastic Film & Sheeting*, 35(3):218–238, 7 2019.
- ⁹, F. C. Krebs. Fabrication and processing of polymer solar cells: A review of printing and coating techniques. *Solar Energy Materials and Solar Cells*, 93(4):394–412, 4 2009.
- ¹⁰, E. Pascual San José. *On the upscaling of organic solar cells based on non-fullerene acceptors*. PhD thesis, Institut de Ciència de Materials de Barcelona, Bellaterra, 2020.
- ¹¹, K. Norrman, A. Ghanbari-Siahkali, and N. B. Larsen. 6 Studies of spin-coated polymer films. *Annual Reports Section "C" (Physical Chemistry)*, 101:174, 2005.
- ¹², J. H. Lai. An investigation of spin coating of electron resists. *Polymer Engineering and Science*, 19(15):1117–1121, 11 1979.
- ¹³, S. A. Jenekhe. The rheology and spin coating of polyimide solutions. *Polymer Engineering and Science*, 23(15):830–834, 10 1983.
- ¹⁴, B. D. Washo. Rheology and Modeling of the Spin Coating Process. *IBM Journal of Research and Development*, 21(2):190–198, 3 1977.
- ¹⁵, B. G. Higgins. Film flow on a rotating disk. *Physics of Fluids*, 29(11):3522, 1986.
- ¹⁶, H. Youn, H. J. Park, and L. J. Guo. Organic Photovoltaic Cells: From Performance Improvement to Manufacturing Processes. *Small*, 11(19):2228–2246, 5 2015.
- ¹⁷, J. George. *Preparation of Thin Films*. CRC Press, 2 1992.
- ¹⁸, Ossila. Glass Substrate Encapsulation Coverslips / Slides | Ossila.
- ¹⁹, S. Y. Chou. Nanoimprint lithography. *Journal of Vacuum Science & Technology B: Microelectronics and Nanometer Structures*, 14(6):4129, 11 1996.
- ²⁰, R. Jiawook and B. Heidari. Nanoimprint lithography and transdermal drug-delivery devices. In *Emerging Applications of Nanoparticles and Architecture Nanostructures*, pages 141–175. Elsevier, 3 2018.
- ²¹, A. Mihi, F. J. Beck, T. Lasanta, A. K. Rath, and G. Konstantatos. Imprinted Electrodes for Enhanced Light Trapping in Solution Processed Solar Cells. *Advanced Materials*, 26(3):443–448, 1 2014.
- ²², X. Chen and L. Zhang. Review in manufacturing methods of nanochannels of bio-nanofluidic chips. *Sensors and Actuators B: Chemical*, 254:648–659, 1 2018.
- ²³, M. Gómez-Castaño, J. L. Garcia-Pomar, L. A. Pérez, S. Shanmugathasan, S. Ravaine, and A. Mihi. Electrodeposited Negative Index Metamaterials with Visible and Near Infrared Response. *Advanced Optical Materials*, 8(19):2000865, 10 2020.
- ²⁴, S. Y. Chou. Sub-10 nm imprint lithography and applications. *Journal of Vacuum Science & Technology B: Microelectronics and Nanometer Structures*, 15(6):2897, 11 1997.
- ²⁵, OrmoStamp. Processing Guidelines - OrmoStamp. Technical report, micro resist technology, Berlin, 11 2012.
- ²⁶, A. Mahmood and J. Wang. A Review of Grazing Incidence Small- and Wide-Angle X-Ray Scattering Techniques for Exploring the Film Morphology of Organic Solar Cells. *Solar RRL*, 4(10):2000337, 10 2020.